applied sciences

MDPI

Article

Performance Analysis of Solar Collector Integrated with Porous Metallic Foam [†]

Vismay Kulkarni [1], Abhishek Singh Kashyap [1], Mayur Pal [2,*] and Himanshu Tyagi [1]

[1] Department of Mechanical Engineering, Indian Institute of Technology Ropar, Rupnagar 140001, Punjab, India; vismaykulkarni.28@gmail.com (V.K.); abhishek.19mez0009@iitrpr.ac.in (A.S.K.); tyagi.himanshu@gmail.com (H.T.)

[2] Department of Mathematical Modelling, Faculty of Mathematics and Natural Sciences, Kaunas University of Technology, 44249 Kaunas, Lithuania

[*] Correspondence: mayur.pal@ktu.lt

[†] This paper is an extended version of our paper published in Kulkarni, V.; Kashyap, A.S.; Pal, M.; Tyagi, H. Numerical Analysis of a Flat Plate Solar Collector Integrated with Porous Copper Foam. In Proceedings of the 26th National and 4th International ISHMT-ASTFE Heat and Mass Transfer Conference (IHMTC-2021), IIT Madras, Chennai, Tamil Nadu, India, 17–20 December 2021.

Abstract: The use of solar energy is a promising solution to reduce dependence on fossil fuels. Flat-plate collectors (FPCs) are commonly employed to harness solar energy, but their performance is often limited by thermal resistance, surface deterioration, and inefficient heat dissipation. This study investigates the performance enhancement of an FPC integrated with porous copper foam through numerical simulations. The porous foam increases surface area and improves heat transfer by creating a complex flow path for the working fluid. Key parameters such as the porous foam height ratio (S), Darcy number (Da), and volumetric flow rate ($\dot{V}$) are analysed to determine their impact on thermal performance. The results indicate that a maximum Nusselt number (Nu) of 28.85 and an outlet temperature of 306.81 K is obtained for $S = 1$. A decrease in Da from 10^{-2} to 10^{-6} and an increase in $\dot{V}$ from 0.25 L/min to 1 L/min enhance the Nu by 5.7% and 8.8%, respectively. The friction factor (f) increases with increases in S, a decrease in Da and an increase in $\dot{V}$. The performance evaluation criteria (PEC) are obtained to be maximum at $S = 0.4$, Da = 10^{-2} and $\dot{V} = 0.25$ L/min. These findings demonstrate the potential of porous copper foam in improving FPC efficiency.

Keywords: solar energy; solar collector; porous foam; metallic insert; heat transfer

Academic Editor: Maria Vicidomini

Received: 8 January 2025
Revised: 12 February 2025
Accepted: 18 February 2025
Published: 24 February 2025

Citation: Kulkarni, V.; Kashyap, A.S.; Pal, M.; Tyagi, H. Performance Analysis of Solar Collector Integrated with Porous Metallic Foam. *Appl. Sci.* **2025**, *15*, 2432. https://doi.org/10.3390/app15052432

1. Introduction

The use of fossil fuels has far-reaching environmental consequences such as increased CO_2 emissions, rising global temperature, the melting of glaciers, oceanic acidification, and heat islands. Even as the ecological and health problems associated with the use of fossil fuels rise, most developed as well as developing countries are still heavily dependent on fossil fuels to meet their energy demand. An alternative is to use clean energy sources such as solar, wind, biomass, etc. It is estimated that an enormous amount of solar energy (about 89 PW; where 1 PW = 10^{15} W) is received on the Earth's surface, even after atmospheric attenuation, which is sufficient to meet the global demand [1]. However, this incident solar energy is of an intermittent nature and lower density; hence, it should be efficiently gathered and harnessed. Mostly, solar thermal collectors are used to harness solar energy in the form of thermal energy. These solar collectors are simply heat exchangers that convert the sun's incident radiation into either thermal or electrical energy. The thermal energy is transferred to the working fluid, which can then be used for applications like space heating or fulfilling domestic or industrial hot water requirements. Broadly, solar collectors are mainly categorized into concentrating and non-concentrating types, depending on the intercepting and absorbing area (i.e., the concentration ratio). The most widely and conventionally used non-concentrating solar collector type is the conventional flat-plate-type collector (FPC), which simply converts the energy of the solar irradiation, incident on the top surface of the collector, into thermal energy (by heating the fluid, generally water).

Moreover, the shortcomings such as high radiative losses, inherent thermal resistance, and the distortion of the spectrally selective coating are encountered with high incident flux, further decreasing efficiency. To enhance the thermal performance of FPCs and minimize losses, various methods have been employed recently, such as the use of nanofluids or insertion of porous media. The use of nanoparticles in the working medium (i.e., nanofluids) augments the heat transfer between the incident solar radiation and the working fluid. This enhancement technique has been widely used in most of the current direct absorption systems [2,3]. There has been significant research on this approach lately [4–9]. Similarly, a lot of work has also been conducted on the insertion of the porous metallic foam in the solar collector [10], which is hereby summarized as follows.

Anirudh et al. [11] performed a numerical investigation to analyse the HTF flow through a permeable cylinder of a square shape. In the investigation, the effect of the variation in Darcy number (Da) and porosity was obtained. The study reported a decrease in boundary layer thickness along with the pressure gradient across the geometry, which resulted in decreasing the inertial and viscous stress offered to the HTF flow. This leads to a suppression in vortex shedding. It is also observed that with the increase in Da, a standing recirculation zone is formed, which results in enhanced heat and momentum transfer. Dhinakaran et al. [12] further investigated the effect of a constant temperature boundary condition on the heat and HTF flow inside a porous cylinder of a square shape. The variation in Da shows that at a lower value of Da (10^{-6}), the cylinder does not allow the HTF to pass through. As the Da is increased, the HTF starts passing through the porous cylinder and results in enhancing the heat transfer. The study also reported that the Nusselt number (Nu) increases with the increase in Da and Reynolds number (Re). With an Re value of 40, the Nu is enhanced by 108.4% at Da of 10^{-2} when compared to the Nu value at Da of 10^{-6}. Srivastava et al. [13] analysed the external and internal heat and mass transfer of a solar still by a modified traditional basin-type single-sloped solar still using blackened cotton cloth porous fins on it. The experimental study shows that during the evening and morning hours, wet porous fins collected most of the solar radiation. The study reported a higher operating temperature and better thermal performance using fins. This was obtained due to the increased evaporation area and low thermal inertia of the design. Also, a lower amount of heat losses at the base and a higher internal heat and mass transfer coefficient was reported compared to that of a traditional solar still. Wu et al. [14] numerically investigated a heated permeable cylinder of a square shape placed in a channel. To obtain the heat transfer, the Darcy–Brinkman–Forchheimer model was taken into account for modelling the porous region. The study reported an increase in heat transfer with the increase in both the Da and channel to cylinder height ratio due to the acceleration provided to the fluid, which passed through the pores. Vijaybabu et al. [15] studied mixed convection (natural and forced) on a heated porous cylinder placed in a horizontal channel. The Brinkman–Forchheimer extended Darcy model was taken for modelling the porous region. Three different ratios of channel height and cylinder (0.1, 0.3 and 0.5) and four values of Da (10^{-5}, 10^{-4}, 10^{-3}, and 10^{-2}) were taken for the investigation. The study reported that at the outlet, by increasing the height ratio and Da, the local Nu increased. This happened due to the acceleration provided to the flow by increasing the height of the cylinder. In another study on mixed convection, Guerroudj et al. [16] investigated two different geometries of porous blocks, i.e., triangular and trapezoidal. Considering the laminar flow through the channel, the porous blocks were situated at the bottom plate, while the top wall was insulated. The Boussinesq approximation for natural convection was taken into account. For the modelling of porous media, the Darcy–Brinkman–Forchheimer extended model was used. Using the finite volume approach, different values of Re (10–300), Richardson's number (0–20), Da (10^{-6}–10^{-1}) and the thermal conductivity ratio (1–10) were taken for numerical solutions. The study reported that triangular blocks with a low value of the studied parameters and rectangular blocks with high values of studied parameters resulted in high heat transfer. Chen et al. [17] performed a numerical simulation to obtain the heat transfer enhancement using a porous layer of high-porosity metal foam. The lower plate was heated using multiple heating sources. This lower plate and heating assembly was placed in an insulated horizontal channel. Three different values of porosity, i.e., 0.85, 0.9 and 0.95, along with pore density values of 5 PPI, 20 PPI and 40 PPI were studied. The study reported a 2 times higher enhancement in the Nusselt number with a low porosity value (0.85) in comparison to a high porosity value (0.95). On the other hand, the high pore density of 40 PPI gives 17% more rise in Nu compared to the low pore density of 5 PPI. In another numerical study, Chikh et al. [18] investigated the heat transfer enhancement in a channel that was filled with the intermittent heating of nine porous blocks. The study reported that by inserting the porous blocks, a decrement of 90% in the wall temperature with a significant enhancement in the local Nusselt number occurred.

An analytical and experimental study on an FPC was performed by Lansing et al. [19]. The study reported that under the same operating conditions, an FPC with porous foam improved the thermal performance of a simple FPC. The improved thermal performance was reported to be 102%. Chen et al. [20] investigated the effect of forced convection on an FPC that was filled with multiple metallic porous blocks. With the assumption of local thermal equilibrium, the Darcy–Brinkman–Forchheimer flow model was employed to the study. The study reported enhanced heat transfer with porous foam. A correlation of the mean Nusselt number with a relative error of 15% was given on the basis of the obtained results. Bovand et al. [21] performed a numerical analysis to obtain the heat transfer enhancement in a solar heater integrated with porous foam. The study reported a 5.9 times increment in the Nu number. In the study, the pressure drop also increased with the increase in the height of the porous layer. Chen et al. [22] investigated the thermal performance of an FPC integrated with aluminium porous foam filled with paraffin wax phase change material. The study reported an enhanced thermal performance with the integrated system in comparison to the system without integration. Rashidi et al. [23] investigated a solar heater by focusing the radiation with the convection heat transfer mode. Re (1 to 100) for fluid flow along with Da (10^{-6} to 10^{-2}) and porous layer thickness (0.33 to 1) were taken as the investigated parameters. The study reported that with an increase in porous layer thickness and keeping Da 10^{-2}, the Nusselt number increased by 96%. It was also reported that the increase in Da reduced the pressure drop. Kumar et al. [24] prepared a methodology to predict the effective, thermal and exergetic efficiencies of a roughened solar air heater with a discrete multi V-pattern rib overheated plate. The investigation consisted of various operating parameters, i.e., Re (2000 to 20,000), Gd/Lv (0.24 to 0.80), g/e (0.5 to 1.5), e/D (0.022 to 0.043), α (30° to 75°), P/e (6 to 12) and a value of W/w in the range of 1 to 10. After optimization, the maximum values of effective efficiency, thermal efficiency, exergetic efficiency and thermohydraulic performance were found to be at the Gd/Lv value of 0.69, g/e value of 1, e/D value of 0.043, α value of 60, P/e value of 8 and W/w value of 6. Anirudh et al. [25] investigated an FPCs' thermal performance by inserting porous foam. The operating parameters such as insolation, permeability and buoyancy were taken to obtain the temperature increment of the flowing fluid. The study reported enhanced thermal performance using porous foam with the effect of the buoyancy force. Chaurasiya and Singh [26] conducted a numerical investigation on a solar air heater with a wavy corrugated design and the impingement of a circular jet array. Geometric parameters in the study were taken as a ratio of the streamwise pitch to hydraulic diameter (X/D_h) in the range of 0.45 to 1.80, a ratio of the spanwise pitch to hydraulic diameter (Y/D_h) in the range of 0.45 to 1.80, a ratio of the jet diameter to hydraulic diameter (D/D_h) in the range of 0.06 to 0.18, duct height h in the range of 0.021 m to 0.046 m, and length of duct L in the range of 0.75 m to 2.25 m. The flow parameter, i.e., Re in the range of 2000 to 26,000, was taken for the investigation. The results demonstrated the best thermohydraulic performance at a 0.45 value of X/Dh, 0.90 value of Y/Dh, 0.06 value of D/Dh, 0.021 m value of h and 18,000 value of Re. Xia et al. [27] conducted a numerical investigation on an FPC integrated with three different shapes of metallic foam blocks. The authors reported that the rectangular-shaped metallic blocks provided the maximum enhancement in comparison to the triangular- and trapezoidal-shaped ones. The thermal performance of the FPC was determined to be increased with an increase in the number of metallic porous foam blocks. The maximum PEC are determined to be 1.68 with six rectangular-shaped metallic porous foam blocks. Dhavale and Lele [28] numerically investigated a heat exchanger with a metallic foam configuration of three different materials with varying porosity and pore density values. The maximum performance parameter value 3.73 was obtained using aluminium porous foam. Considering the solar air heating applications, Al-Chlaihawi et al. [29] performed a numerical simulation on a rectangular channel using metallic foam blocks placed in an intermittent position. The simulation is carried out by varying the permeability and Reynolds number. The study reported that using five porous blocks, the maximum PEC value of 2.71 was obtained, which showed a 171% improvement in thermal performance compared to the empty channel. Variji et al. [30] performed a numerical study to optimize the porous foam structure in the context of obtaining the maximum thermal performance of flat-plate collectors. Geometrical parameters such as the non-dimensional height and length of the rectangular porous blocks were varied to obtain the maximum Nu. An improvement of 7.23% was obtained in Nu using the modified geometry compared to the conventional rectangular blocks with a constant height. Lin et al. [31] carried out a numerical study on a flat-plate collector with porous media and nanofluids. A maximum PEC value of 1.8 was obtained using rectangular porous blocks with a 3% mass concentration of nanofluid.

With global warming and climate change on the rise, developed and developing countries are relying on renewable energy. Amongst the various viable options, solar energy is the most important resource. The current FPC technology has been the long-standing state-of-the-art means to harness solar energy. The working mechanism of an FPC takes place with two heat transfer mechanism conductions through the absorber plate and then convection to the HTF. During the heat transfer between the absorber plate and HTF, there exists thermal resistance, which results in reducing the thermal efficiency. To increase the thermal efficiency or obtain a high HTF temperature at the outlet, a higher heat flux can be provided to the absorber plate, but on the other hand, it can deteriorate the selective coating material of the absorber plate [32]. Moreover, a significant temperature gradient exists between the absorber plate and the HTF, which also contributes in reducing the thermal efficiency of the FPC. These limitations regarding low thermal efficiency restrict FPC application in low temperature ranges, i.e., space heating, low-temperature domestic and industrial water heating.

Hence, in recent times, various techniques have been explored to reduce the losses and improve the performance in FPCs. Another attractive performance enhancement method in FPCs is the use of porous media. This study aims at further enhancing the performance of typical FPCs by adding a metallic porous foam. This kind of collector, if scaled, can be used for both domestic and commercial applications such as household requirements, district heating, industrial hot water requirement, etc.

Porous media are multiphase materials that contain pores or voids within a fixed solid skeletal portion called the frame or matrix. A solid matrix and the pores are uniformly distributed within a fixed volume [33]. In the given arrangement, the HTF (either in a single phase or in multi phases) flows through the pores. The additional surface area provided from the solid matrix promotes the HTF flow mixing and increases the heat transfer between the solid matrix and HTF. This heat transfer enhancement advantage of using the porous media makes it interesting to integrate porous media with an FPC.

Hence, from the literature review conducted, it can be understood that the inclusion of porous foam provides an additional surface area for the transfer of heat and enhances thermal mixing, owing to the tortuous interconnected path provided to the flow of the working fluid. The porous foam helps to efficiently transfer the heat from the absorber plate to the working fluid, thereby improving thermal performance. The regular development of a flat-plate collector integrated with metallic porous foam is one of the most focused areas among researchers. As the literature shows that different configurations of porous blocks along with the size and position are some of the key factors that can improve the thermal performance of the system, the present numerical investigation is carried out to obtain the effect of varying the height (S) of the metallic (copper) porous foam.

Porous media provide interconnected tortuous paths for the flow of working fluid. Additionally, the structural arrangement of the porous foam increases the contact area, which in turn promotes mixing, reduces thermal resistance, minimizes losses, and enhances the heat transfer. Hence, the main focus of this study is to investigate the potential of porous media as a performance enhancer in the case of an FPC. To accomplish this objective, a numerical analysis is performed to find the best values of three essential parameters, i.e., Nu, f and PEC, by varying the geometric and operating parameters, i.e., S, Da and $\dot{V}$.

2. Description of the Physical System

2.1. Flat-Plate Solar Collector

A schematic of a typical flat plate is shown in Figure 1. The FPC mainly consists of an absorber plate, glazing surface (glass cover), circulating working fluid, and insulation at the bottom. The glazing surface consists of a single or multiple sheets of the glass cover. As shown in the figure, the glass cover is placed above the absorber plate. The working fluid employed in the FPC is almost transparent to incident solar radiation and therefore is not able to absorb the sunlight by itself [34].

The absorber plate is a metallic spectrally selective surface that absorbs the incident solar radiation and transfers it to the working fluid. The spectrally selective coatings employed in the FPC generally have very high absorptivity in the visible and near-infrared (IR) portions of the spectrum (0.5–2.5 μm) and low emissivity in the mid-infrared (IR) region of the spectrum (2.5–10 μm), which makes the FPC a promising way of harnessing energy [35]. Commercially available TiNOX-coated copper or aluminium substrate is commonly employed as the material for spectrally selective coating.

The glass cover helps minimize heat losses (convective and radiative) from the absorber plate to the surrounding. The insulation is provided at the bottom of the FPC to reduce the heat losses from the working fluid to the surrounding by conduction.

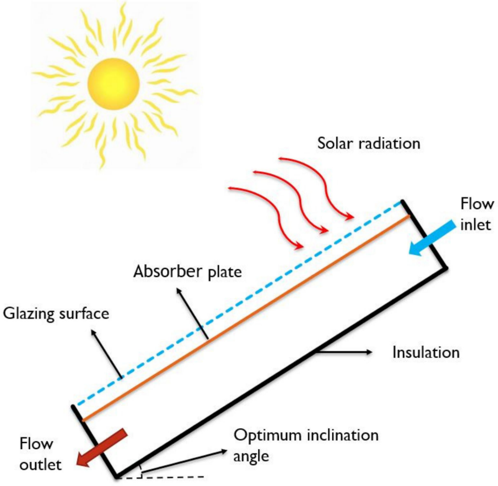

Figure 1. A schematic of an FPC consisting of various components viz. the absorber plate, glazing surface, working fluid and insulation.

2.2. Porous Media

In order to understand the flow physics and heat transfer taking place through porous media, we will first look at the essentials of porous media. The most fundamental term related to porous media is volumetric porosity, ε, which is defined as the ratio of the volume occupied by the pores to the total volume of the media and is given by the following expression:

$$\varepsilon = \frac{Vol_{pores}}{Vol} \tag{1}$$

The volumetric porosity is reduced to surface porosity in the two-dimensional scenario. The governing equation for the flow of fluid through the porous media was coined by Henry Darcy, based on their experimental work of filtering wastewater through sand in hospitals. The proposed relation gives a correlation between the instantaneous rate of discharge and the pressure drop. This provides an expression for the hydraulic conductivity of the porous medium, δ, which is defined as follows [36].

$$\delta = \frac{U}{\frac{\Delta P}{L}} \tag{2}$$

Here, δ is the hydraulic conductivity, U is the average fluid speed, and ΔP is the pressure difference across the porous medium layer of length L. Darcy law was further refined to the well-known form as below.

$$\frac{\Delta P}{L} = \left(\frac{\mu}{\kappa}\right)U \tag{3}$$

In this equation, μ is the dynamic viscosity of fluid, and κ is the permeability of the porous region, which represents the ease with which the fluid can flow through a permeable porous region. Permeability is also the hydraulic property of a porous medium. The term is further non-dimensionalized by dividing it by the square of the characteristic dimension, D_h (hydraulic diameter in the case of a pipe or duct flow), which gives Da.

$$\mathrm{Da} = \frac{\kappa}{{D_h}^2} \tag{4}$$

Darcy law is applicable to viscous flow, i.e., for flow with an Re less than 10. However, for the cases where inertial effects become relatively significant, an additional term needs to be introduced in the Darcy equation called the Forchheimer term. The modified equation is expressed as below.

$$\frac{\Delta P}{L} = \left(\frac{\mu}{\kappa}\right) U + C\rho U^2 \tag{5}$$

Furthermore, there also exists shear and viscous resistance within the porous region, at the interface of the solid and liquid. In order to account for interfacial shear between the solid phase and the fluid, Brinkman proposed an additional term. The refined equation considering Brinkman's term can be written as follows:

$$\nabla P = \mu \nabla^2 \vec{U} + \left(\frac{\mu}{\kappa}\right) \vec{U} \tag{6}$$

After combining all the above information for flow through porous media, the momentum equation in the porous region is expressed as below [37].

$$\rho \left[\frac{1}{\varepsilon} \frac{\partial \vec{U}}{\partial t} + \frac{1}{\varepsilon} \vec{U} . \frac{1}{\varepsilon} \nabla \vec{U} \right] = -\nabla P + \mu \nabla^2 \vec{U} - \left(\frac{\mu}{\kappa}\right) \vec{U} - C\rho |\vec{U}| . \vec{U} \tag{7}$$

The above equation is a modified form of the Navier–Stokes equation with three additional source terms (Brinkman, Darcy, and Forchheimer). This modified momentum equation as expressed in Equation (7) is applicable for flow through porous media. In the above equation, the first term is the Brinkman coefficient, which considers the shear and viscous resistance. The second term is the Darcy term, which considers the existence of general porous resistance in the direction of flow. The third term is the Forchheimer term, which accounts for inertial resistance to the fluid flow (caused by the porous medium). On the other hand, the flow in the clear fluid region, i.e., outside the porous area, is modelled by the general Navier–Stokes equation (with no additional source terms). The permeability (κ) and the Forchheimer coefficient (C) can be defined with the help of Carman–Kozeny and Ergun relations as follows [21].

$$\kappa = \frac{dp^2 \varepsilon^3}{180\ (1-\varepsilon)^2} \tag{8}$$

$$C = \frac{1.75\ (1-\varepsilon)}{d_p \varepsilon^3} \frac{1}{\sqrt{\kappa}} \tag{9}$$

It is expected that adding porous foam inside the FPC may improve its performance, primarily due to greater mixing as well as a higher effective surface area for heat transfer. With the inclusion of porous media, the incident radiation can traverse only a small distance before it is absorbed or scattered completely. This causes the optical thickness of the medium to increase, thereby helping to solve the radiative transfer equation (RTE), which depends mainly on the position and direction. Generally, to model an optically thin medium, radiation models such as the Discrete Ordinate Method (DTRM) and Finite Volume Discrete Ordinate Method (fvDOM) are considered. In these methods, providing solutions for radiation intensity involves discretization in both the space and direction of radiation propagation, which becomes computationally expensive and time-consuming [38]. However, if the porous media with homogenous and isotropic properties are inserted in the FPC, then we can use the popular P1 radiation model. This model is suitable for optically thick medium, such as in our case, which requires relatively lower computational demand, less time, and reasonably accurate results [39]. The P1 radiation model is a first-order approximation of the general PN model. This first-order approximation method converts the integral terms present in the radiative transfer equation (RTE) to differential terms through a set of moment equations. Thus, the radiant transfer equation is reduced to the following form [40], where τ represents the optical thickness of the medium, and $J(x, y)$ indicates the irradiance.

$$\nabla . q_r = \tau \left[4T^4 - J(x, y) \right] \tag{10}$$

The differential moment equation to define irradiance is given by

$$\nabla^2 J = 3\tau^2 \left[J(x, y) - 4T^4 \right] \tag{11}$$

Now, the numerical study can be conducted with the understanding of FPCs, porous media, momentum equations, and radiation models. For the purpose of the numerical simulation, CFD-based Open-Source Field Operation and Manipulation (OpenFOAM 5.0) software is used in this study. This software is based on the C++ framework, and it is suitable to carry out a numerical simulation based on the finite volume method (FVM). The literature suggests that the network modelling of porous media may affect the heat transfer as per the application [41]. In this study, however, the focus is on the performance enhancement of the FPC with the use of metallic porous media under the assumption of a uniform pore size (the porous foam is considered to be homogenous and isotropic). Metallic porous foam has a wide range of applications in heat exchangers, industrial cooling and thermal energy storage applications. The present investigation is carried out to explore the effect of geometrical parameters such as the Darcy number (Da) to see the effect of the pore size and channel to porous media height ratio (S) in the context of heat transfer augmentation in an FPC integrated with metallic porous media. In the present study, the radiation models are not considered, and a simple heat transfer case is considered to simplify the analysis. The numerical analysis is performed for a 2D steady-state, laminar, and incompressible flow of fluid through a channel inside the solar collector. The investigation is carried out under a constant heat flux condition, with water as the working fluid. The porous region is modelled utilizing the Darcy–Brinkman–Forchheimer model and by considering local thermal equilibrium (LTE) within the various phases inside the collector channel.

3. Mathematical Model of the System

The primary focus of this study is to investigate the effect of using a porous metallic foam on the overall thermal performance of a flat-plate collector [10]. Hence, in this study, the thicknesses, as well as optical properties of both the glass cover and absorber plate, are neglected. Both the absorber plate and glass cover are considered to be a single layer, and its thickness is ignored in the present numerical endeavour. This assumption can be safely made, keeping in mind the focus of the study. This assumption has similarly also been made in similar numerical studies on FPCs with porous foam insertion [21,23,42]. Further, the porous metallic foam is assumed to have homogenous properties and is assumed to be in local thermal equilibrium (LTE) with the fluid. This assumption can be safely considered in the situation where the slow heating of working fluid takes place, as in the present case. The present numerical investigation focuses on the heat transfer aspect of a flat-plate collector. In a real scenario, the heat flux changes throughout the day. For simplifying the numerical model, a constant heat flux value of 1000 $\mathrm{W/m^2}$ is considered. In the real case, gravity plays a significant role and the tilt angle provided to a flat plate collector is also important. However, in the present investigation, a simple case of a horizontal flat-plate collector is studied numerically by neglecting the buoyancy forces and tilt angle as the height of the fluid flow channel is taken to be relatively smaller (0.013 m) in comparison to the length (0.8 m). In a flat-plate collector, heat losses occur because of airflow above the absorber plate. Glazing is provided to reduce such heat losses. However, in this simple model of a flat-plate collector, the convection losses are neglected. In the future, they may be considered.

The porous metallic foam is also assumed to have uniform permeability and porosity (in all directions, i.e., isotropic). A flat-plate collector is configured such that it is irradiated by a flux of 1000 $\mathrm{W/m^2}$ from the normal to the top surface. The incident flux is uniformly distributed along the channel's entire length, and its value is kept constant throughout the numerical simulations.

The thickness and optical properties of both the glass cover and absorber plate are assumed to be neglected, and hence, losses are not considered. The channel height (H) and length (L) of the flat-plate collector are 0.013 m and 0.8 m, respectively. The present model shows a variation in the thickness of porous media by considering that the variable S ranges from 0 to 1. At S = 1, the top boundary condition becomes the porous foam boundary condition. From S = 0 to 0.8, the heat transfer takes place from the absorber plate to the working fluid and then porous media. At the top boundary, as shown in Figure 2, the thermal conductivity of fluid (k_f) is considered because the heat transfer is taking place from the absorber plate to the working fluid. For the metal porous foam, the effective thermal conductivity (k_{eff}), defined in Equation (13), is used to incorporate the overall effect of both solid- and liquid-phase thermal conductivities.

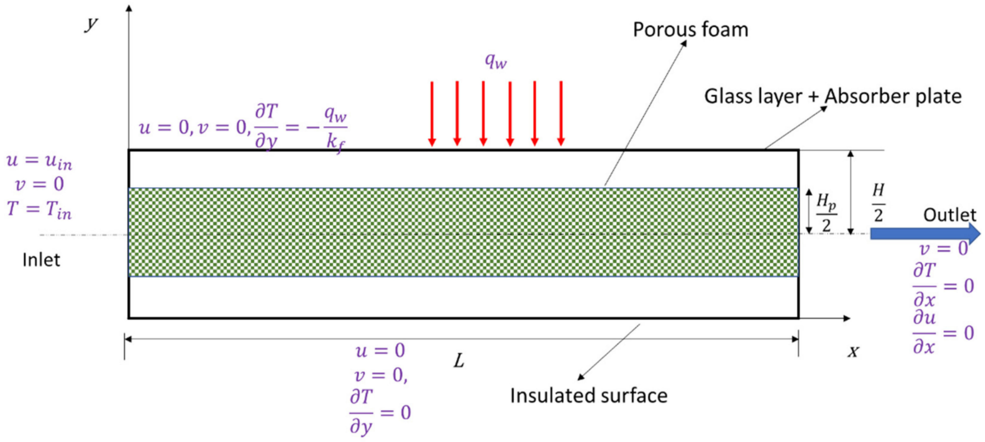

Figure 2. A schematic of the system that is modelled in this study.

In the case of fluid flow in a clear region (i.e., in the region without porous foam), the governing equations are given by the conventional continuity (the conservation of mass) and Navier–Stokes equations (the conservation of momentum). However, due to the presence of the porous region (within the flat-plate collector channel), such equations can be directly implemented in the porous region, and few alterations are needed in them. This process is described as follows. The superficial velocity of flow in the porous region is the artificial velocity of flow by which the fluid flow will occur in the absence of the porous region (i.e., empty channel). In simple terms, it is the flow velocity when the presence of the porous region is not considered. It is known that due to the inclusion of porous foam, the area available for fluid flow decreases, which causes an increase in the velocity of fluid coming out through the pores, which is referred to as actual or physical velocity. The superficial velocity of flow is relatively easy to determine. In contrast, the actual velocity (also referred to as physical velocity) is challenging to determine, and it depends on the location within the porous region. Hence, the actual velocity is higher than the superficial velocity in the porous region. The actual and superficial velocity can be linked with the help of porosity, ε, as below.

$$\bar{s} = \frac{u}{\varepsilon} \tag{12}$$

where $\bar{s}$ is the velocity of the fluid in porous region. Hence, to model flow in the porous region, an additional term $1/\varepsilon$ is added next to the velocity term in the governing equation. Further, to incorporate the thermal conductivity of metal porous foam, the effective thermal conductivity (k_{eff}) of the porous media in terms of fluid and solid thermal conductivities (k_f and k_s) is defined as follows [43].

$$k_{eff} = A\left(\varepsilon k_f + (1-\varepsilon)k_s\right) + \frac{1-A}{\left(\frac{\varepsilon}{k_f} + \frac{1-\varepsilon}{k_s}\right)} \tag{13}$$

During the fluid flow, different resistances acting on the fluid are modelled by adding three source terms in the momentum equation. The solid matrix imposes the porous resistance to the fluid flow, shear resistance acts at the solid–liquid boundary in the porous region and the inertial resistance acts on the fluid flow by the porous media. These three resistances are modelled using Darcy, Brinkman and Forchheimer source terms sequentially in the momentum equation. This approach is called as the Darcy–Brinkman–Forchheimer extended model. As the literature shows, this model is majorly used in many research papers. After considering all the source terms, the governing equations are modified and solved as given below:

Momentum equation(s):

$$\frac{\rho}{\varepsilon^2}\left(u\frac{\partial u}{\partial x} + v\frac{\partial u}{\partial y}\right) = -\frac{\partial p}{\partial x} + \frac{\mu}{\varepsilon}\left(\frac{\partial^2 u}{\partial x^2} + \frac{\partial^2 u}{\partial y^2}\right) - \frac{\mu}{\kappa}u - \frac{\rho C}{\sqrt{\kappa}}\left|\vec{V}\right|u \tag{14}$$

$$\frac{\rho}{\varepsilon^2}\left(u\frac{\partial v}{\partial x} + v\frac{\partial v}{\partial y}\right) = -\frac{\partial p}{\partial y} + \frac{\mu}{\varepsilon}\left(\frac{\partial^2 v}{\partial x^2} + \frac{\partial^2 v}{\partial y^2}\right) - \frac{\mu}{\kappa}v - \frac{\rho C}{\sqrt{\kappa}}\left|\vec{V}\right|v \tag{15}$$

Energy equation:

$$\frac{1}{\varepsilon}\left(u\frac{\partial T}{\partial x} + v\frac{\partial T}{\partial y}\right) = \alpha\left(\frac{\partial^2 T}{\partial x^2} + \frac{\partial^2 T}{\partial y^2}\right) \tag{16}$$

The flow velocity, temperature, and horizontal and vertical distances are non-dimensionalized using inlet velocity, inlet temperature, wall temperature and channel dimensions as follows.

$$x^* = \frac{x}{L},\ y^* = \frac{y}{H},\ u^* = \frac{u}{u_{in}},\ v^* = \frac{v}{u_{in}},\ \theta = \frac{T - T_{in}}{T_w - T_{in}} \tag{17}$$

At the outlet of the channel, the local Nusselt number is calculated as shown by Equation (18) [25,42].

$$Nu_L = \frac{k_{eff}}{k_f}\left(\frac{D_h}{T_w - T_m}\left(\frac{\partial T}{\partial y}\right)_{y=H}\right)_{x=L} \tag{18}$$

where D_h is the hydraulic diameter, T_w is the wall temperature and T_m is the mean temperature at location $x = L$. The values of D_h and T_m are calculated as follows:

$$D_h = \frac{4A}{p} \tag{19}$$

$$T_m\,(x) = \frac{\int_{y=0}^{y=H} u\,T\,dy}{\int_{y=0}^{y=H} u\,dy} \tag{20}$$

As the figure shows, the fluid enters the inlet at a uniform temperature (T_{in}) and uniform velocity (u_{in}). The flow takes place in the x-direction only by considering the y-direction component to be zero. While passing through the channel, the fluid flow becomes fully developed before reaching the outlet. It can be said that with time, there is no change in the velocity profile at the outlet. As per the given "InletOutlet" boundary conditions in OpenFOAM, $v = 0$, $(\partial u)/(\partial x) = 0$ is applied at the outlet of the channel.

Using the abovementioned boundary condition at the outlet, the reverse flow of the fluid is prevented by setting the velocity at zero ($v = 0$) along with providing a fully developed flow condition. The zero-gradient boundary condition ($(\partial T)/(\partial x) = 0$) extrapolates the nearest cell's temperature quantity to the outlet. A uniform heat flux boundary is applied at the top of the absorber plate, which defines the Neumann boundary condition as the temperature gradient $(\partial T)/(\partial y) = -q_w/k_f$. The no-slip boundary $u = v = 0$ is applied to the velocity field. At the bottom of the FPC, the insulated boundary condition $(\partial T)/(\partial y) = 0$ and no-slip boundary condition $u = v = 0$ are applied. In this study, to numerically analyse the flow and heat transfer in a flat-plate collector channel integrated with porous metal foam, the finite volume method (FVM) is adopted. The numerical solver is based on the SIMPLE algorithm. The Darcy–Forchheimer–Brinkman extended model is used in this study to model the porous region. The steady-state scheme is employed to manage the time derivative. In order to solve the gradient, divergence, and Laplacian terms, the Gauss linear scheme is chosen as it is second-order accurate. The linear interpolation scheme is selected in this study to evaluate the face values from the values calculated at the centre of the node. Further, the pressure term is calculated with the help of the Newton–Krylov PCG solver along with a pre-conditioner since it is suitable for solving symmetric matrices. For solving the velocity and the temperature terms, the Newton–Krylov PBiCG solver (suitable for asymmetric matrices), along with a pre-conditioner, is used. In order to have minimal errors in the numerical solution, the residual is kept equal to a very low value of 10^{-6} for the pressure, velocity, and temperature term. The under-relaxation values for pressure, velocity, and temperature are chosen based on the literature review as 0.3, 0.7, and 0.98.

Validation and Grid Independence

To proceed with the numerical simulation, a validation of the written code is performed considering the available studies by Morosuk [44] and Mohamad [45]. In both studies, the channel is taken to be partially and fully occupied by porous media. A rectangular channel of 0.8 m length and 0.026 m height is discretized in 91 × 160 mesh elements. Different values of Da and porous media thickness are taken as the variables. A constant temperature is maintained at the wall of the channel. The schematic, along with the boundary conditions of the investigated model for code validation, is shown in Figure 3.

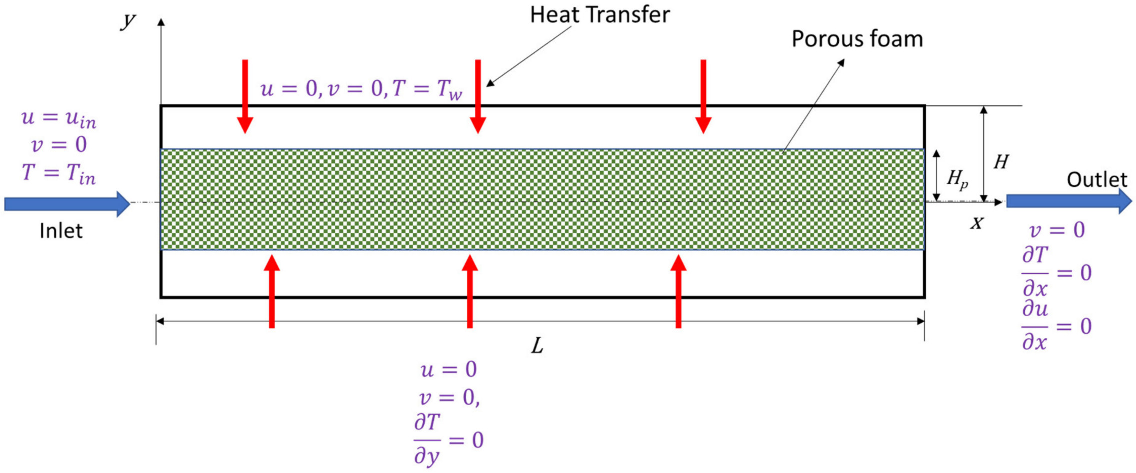

Figure 3. A schematic of the arrangement along with the boundary conditions (for code validation). The working fluid enters from the left and leaves the channel from the right.

For validation, water is taken as the working fluid that flows inside the channel under certain assumptions, i.e., the flow is laminar, incompressible and steadily two-dimensional. The Reynolds number for the flow is taken to be 130. As shown in the figure, the boundary conditions are taken as mentioned in the above section, i.e., uniform velocity and temperature of the inlet, a constant wall temperature with a no-slip boundary at the wall and zero velocity and temperature gradient at the outlet of the channel. An axis is defined at the centreline of the domain. For the validation, the velocity and temperature fields are validated with Morosuk [44], and the pressure drop is validated with Mohamad [45]. Numerical simulation is performed for the Da values of 10^{-2} and 10^{-6} and channel fill ratio S (defined by Equation (21)) values of 0.2, 0.4, 0.6, 0.8, and 1.

$$S = \frac{H_p}{H} \tag{21}$$

where H_p is the height of the porous media and H is the height of the channel. Temperature, velocity and distance in the y-direction are non-dimensionalized, corresponding to inlet temperature, inlet velocity and channel height. Regarding the results, temperature and velocity curves are plotted for different values of S. The validated results for the non-dimensional temperature profile, non-dimensional velocity profile and non-dimensional pressure drop are presented in Figures 4–6, respectively. The results obtained from the present study show very satisfactory agreement with the results from Morosuk [44], with a maximum error of 4%.

To validate the pressure drop calculations, pressure drop and distance in the y-direction are non-dimensionalized, as shown in Equation (22). The numerical results are obtained for the Da values of 10^{-2}, 10^{-3}, 10^{-4}, and 10^{-5} and S values of 0.2, 0.4, 0.6, and 0.8.

$$P^* = \frac{P}{\rho u^2} x^* = \frac{L}{\frac{H}{2}} \tag{22}$$

For all the values of Da and S, the non-dimensional pressure drop is presented in Figure 6. The obtained plots show good agreement with the results from Mohamad [45], with a maximum error of 6%.

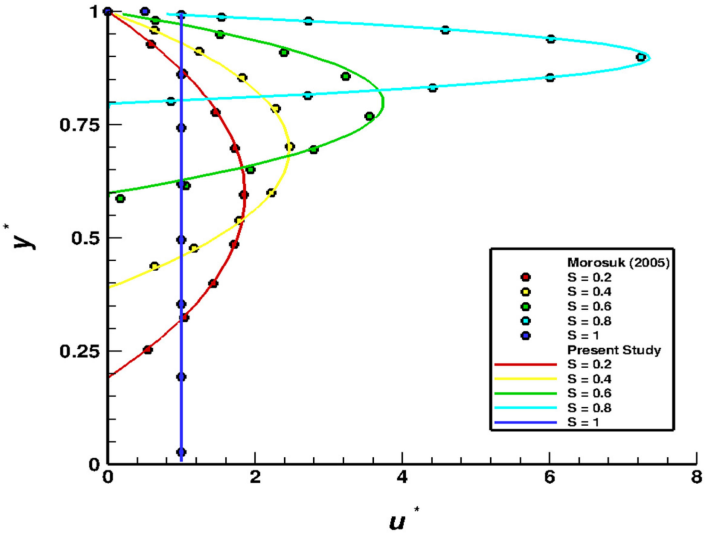

Figure 4. A comparison between the non-dimensional velocity profiles at the outlet of the collector channel for Da = 10^{-6} for the purpose of the code validation [44].

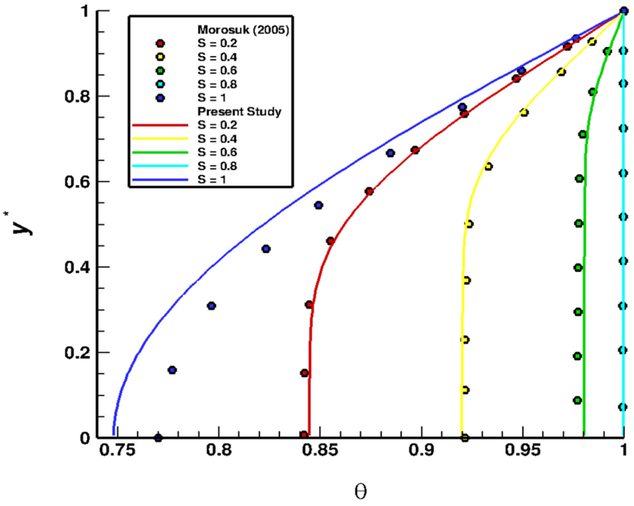

Figure 5. A comparison between the non-dimensional temperature profiles at the outlet of the collector channel for Da = 10^{-6} for the purpose of the code validation [44].

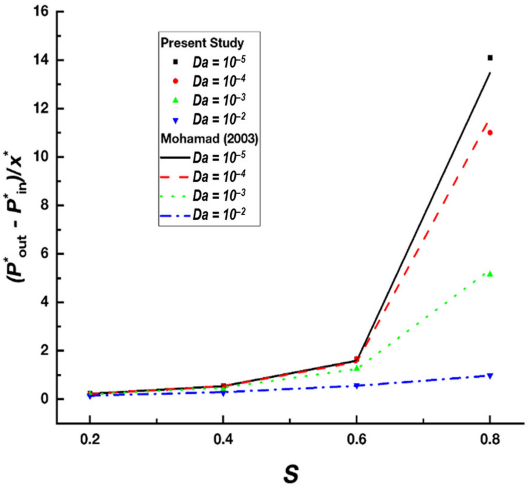

Figure 6. A comparison between the non-dimensional pressure drop for various values of S and Da for the purpose of the code validation [45].

Further, a grid independence test is performed to carry out the numerical simulations with accuracy. The meshing is performed in OpenFOAM 5.0 using the blockmesh tool. With the help of this tool, a uniform and simple graded orthogonal mesh is created for the channel. Extreme cases of simulations (where the results are affected considerably) are taken into account to obtain the grid independency. The grid independence test is conducted for a different number of elements to obtain the Nu, using $S = 1$ and Da = 10^{-4}. The results of the grid independence are presented in Table 1. By taking the low relative error into consideration, 87,500 elements with a distribution of a 350 × 250 grid size in the X and Y directions are used for all further numerical analyses.

Table 1. Grid independence test with obtained values of relative error in Nusselt number.

Number of Elements	Nu	Relative Error (%)
20,000	29.01	0.97
37,500	28.96	0.49
60,000	28.88	0.23
87,500	28.85	0.11

4. Results and Discussion

4.1. Nusselt Number (Nu)

With increasing value of S, the Nusselt number increases significantly, as seen in Figure 7a. For values of S corresponding to 0, 0.2, 0.4, 0.6, 0.8, and 1, the Nusselt numbers obtained are 5.46, 8.67, 11.92, 16.68, 24.54, and 28.85, respectively. The increase in Nusselt numbers up to $S = 0.8$ is primarily due to the channelling effect, which enhances heat transfer by aiding the removal of heat from the absorber plate. Further, the high thermal conductivity of the porous metal foam contributes to improved heat transfer. When $S = 1$, the channelling effect diminishes; however, the high thermal conductivity and increased surface area of the foam dominate. This results in the improved Nusselt number value of 28.85. Therefore, a fully filled porous foam channel ($S = 1$) is identified as the optimal configuration for further investigation.

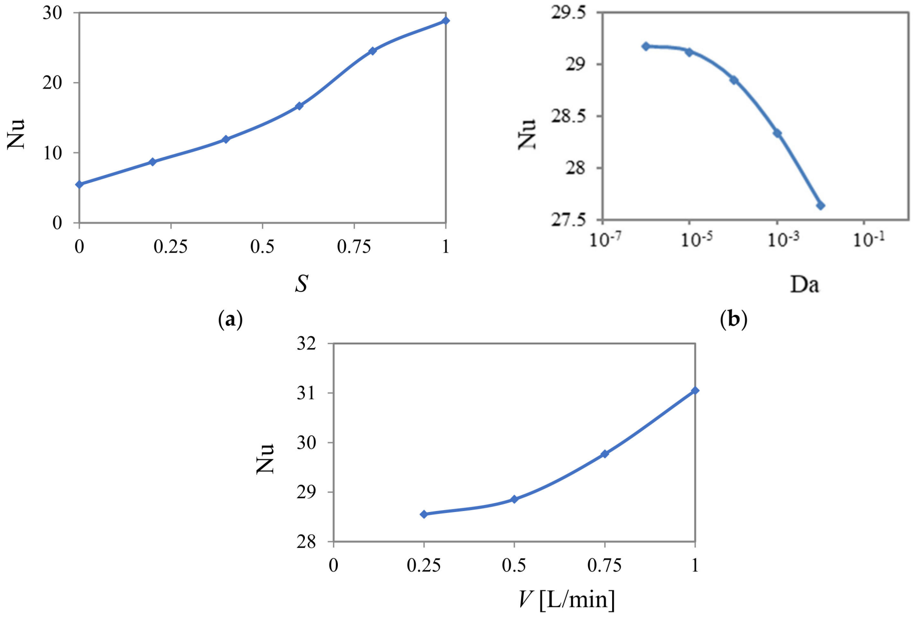

(**a**) (**b**)

(**c**)

Figure 7. Plot of Nusselt number (Nu) as a function of (**a**) the channel fill ratio (S), (**b**) Darcy number (Da), and (**c**) volumetric flow rate ($\dot{V}$).

The Nusselt number variations with the non-dimensional Da are shown in Figure 7b. The Nusselt number increases significantly as Da decreases from 10^{-2} to 10^{-6}, with values of 27.63, 28.33, 28.85, 29.12 and 29.17, respectively. The smallest increment from 29.12 to 29.17 is observed as Da decreases from 10^{-5} to 10^{-6}, representing a total enhancement of 5.6%. This improvement is due to the reduced temperature difference between the top absorber plate and the mean outlet temperature as Da decreases. In a channel filled with porous foam, heat conduction dominates. As Da decreases, the particle (or fibre) diameter becomes smaller, increasing the solid–fluid interfacial area and enhancing heat transfer. Consequently, the maximum Nusselt number 29.17 is achieved at a Da value of 10^{-6}.

Further, the local Nusselt number at the channel outlet is calculated for each volumetric flow rate, as shown in Figure 7c. The results show an exponential increase in the Nusselt number with an increase in flow rates. Nusselt number values of 28.54, 28.85, 29.78, and 31.05 are observed for flow rates of 0.25, 0.5, 0.75, and 1 L/min, respectively. This shows an 8.8% improvement in the Nusselt number as the flow rate increases from 0.25 L/min to 1 L/min. Additionally, higher flow rates increase the velocity gradient near the absorber plate, improving heat transfer through convection (as per Reynolds' analogy). The temperature difference between the absorber plate and the mean outlet temperature decreases with rising flow rates, while the temperature gradient at the outlet increases, leading to the highest Nusselt number of 31.05 at 1 L/min.

4.2. Friction Factor (*f*)

It is understood from the present numerical study that the heat transfer performance of FPCs is enhanced by the use of porous copper foam, mainly due to an augmentation in heat dissipation. However, this performance improvement also involves an unfavourable rise in pressure drop in the flow direction, resulting in an increase in pumping power. Hence, it is crucial to evaluate the increment in pressure drop resulting from the insertion of porous foam so that the efficient utilization of the available energy is carried out with no significant increase in the pumping power. In this study, the pressure drop is evaluated in terms of the non-dimensional friction factor using the following expression [23].

$$f = \frac{-2\, D_h\, \Delta P}{\rho\, u^2\, L} \tag{23}$$

The friction factor is evaluated for the six cases studied earlier corresponding to various values of the channel fill ratio (S). The values of channel fill ratio is varied from 0 (empty channel), 0.2, 0.4, 0.6, 0.8, and 1 (completely filled channel), and its effect on the friction factor is obtained using Equation (23). The values of the other operational parameters are kept the same as before, i.e., u = 0.009 m/s and L = 0.8 m. The hydraulic diameter is calculated based on the cross-sectional dimensions. The variation in the friction factor as a function of the channel fill ratio (S) is shown in Figure 8a.

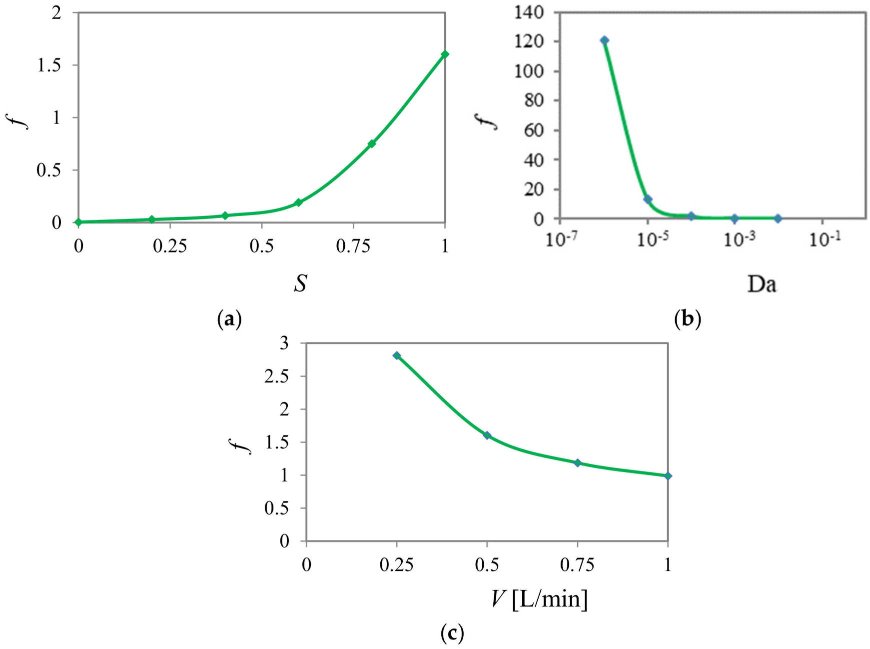

(**a**) (**b**) (**c**)

Figure 8. Plot of friction factor (f) as a function of (**a**) the channel fill ratio (S), (**b**) Darcy number (Da), and (**c**) volumetric flow rate ($\dot{V}$).

This figure shows that the value of the friction factor increases quite rapidly with an increase in the height of the porous foam from S = 0 to S = 1. The values of the friction factor corresponding to values of S = 0, 0.2, 0.4, 0.6, 0.8, and 1 are 0.004, 0.03, 0.07, 0.19, 0.75, and 1.61, respectively. This can be attributed to the fact that as the value of S increases, the value of the friction factor (f) increases as the working fluid has less space to escape without encountering the porous medium. Hence, the increase in macroscopic bulk and microscopic interstitial drag forces causes an increase in the friction factor.

Further, to determine the variation in pressure drop with Da, the friction factor is evaluated for the optimum case, i.e., completely filled channel (S = 1). The variation in the friction factor with the Da is carried out in the range 10^{-6} to 10^{-2}, as shown in Figure 8b. As seen in this figure, the value of f (friction factor) decreases rapidly from 120.7 to 0.0637 with an increase in Da. The values of the friction factor obtained are 13, 1.6, and 0.26 for the values of Da equal to 10^{-5}, 10^{-4}, and 10^{-3}, respectively. This is because as the Da increases, both inertial and viscous resistances offered by the porous foam to the working fluid decreases, causing a decrease in f (friction factor). Hence, as the porous foam becomes more porous, the friction factor decreases rapidly.

The value of the friction factor is further evaluated for different values of the volumetric flow rate (between the range of 250 mL/min, and 1000 mL/min), and the results are shown in Figure 8c. The friction factor is seen to decrease rapidly with the volumetric flow rate. The values of the friction factor are 2.8, 1.6, 1.2, and 0.99, corresponding to the volumetric flow rates of 250, 500, 750, and 1000 mL/min, respectively. As the volumetric flow rate increases, the resistance offered by porous foam becomes comparable with the surface friction, causing a significant drop in the friction factor.

4.3. Performance Evaluation Criteria (PEC)

As seen in the previous section, the inclusion of the porous foam in the FPC channel incorporates an additional pressure penalty. Though having a positive effect on enhancement in heat transfer, the presence of the porous metallic foam leads to a greater pressure drop. Hence, in order to quantify the efficacy of adding this porous metallic foam, a term called the performance evaluation criteria (PEC) is introduced, which are evaluated as follows [23].

$$\mathrm{PEC} = \frac{\frac{Nu_p}{Nu_e}}{\left(\frac{f_p}{f_e}\right)^{1/3}} \tag{24}$$

This term takes into account both the improvement in thermal performance through Nu (Nusselt number) and increment in pumping power through f (friction factor). The expression for PEC considers the enhancement in Nu and increment in f (friction factor) in the porous channel (represented by the subscript p) relative to the empty channel case (represented by the subscript e) corresponding to S = 0. The PEC are evaluated for all the five cases corresponding to the values of S = 0.2, 0.4, 0.6, 0.8, and 1 using Equation (24) with respect to the S = 0 case, and this is represented in Figure 9a.

The value of the PEC first increases with an increase in the height of porous foam from S = 0.2 to 0.4, reaches a maximum value of 0.875 at S = 0.4, and then decreases up to S =1. The values of the PEC are about 0.84, 0.88, 0.86, 0.80, and 0.73 for the values of S = 0.2, 0.4, 0.6, 0.8, and 1, respectively. For all the cases, the value of the PEC is less than 1, which indicates that the increment in pumping power is relatively higher compared to the expected enhancement in the Nusselt number. Hence, if there is no limitation on the pumping power, then the optimum arrangement can be considered the same as earlier, i.e., S = 1. However, if the pumping power is to be considered, then the optimum arrangement corresponds to S = 0.4 cases where the highest value of the PEC is obtained.

Furthermore, the PEC were evaluated corresponding to different values of Da to study their variation with changes in permeability. Five values of Da viz. 10^{-6}, 10^{-5}, 10^{-4}, 10^{-3}, and 10^{-2} were considered in the study. The variation in the PEC with Da is as shown in Figure 9b. For preparing this plot, the value of the channel fill ratio, S, is held constant at 1. As the Da increases from 10^{-6} to 10^{-2}, the PEC also increase linearly with a value of 0.17 to 2.05. The value of the PEC is about 0.37, 0.73, and 1.32 at Da equal to 10^{-5}, 10^{-4}, and 10^{-3}, respectively. As the value of Da increases, the enhancement in the Nu is more prominent compared to the increment in f (friction factor). Therefore, the value of the PEC increases with Da and reaches a maximum value of 2.05 at a Da of 10^{-2}.

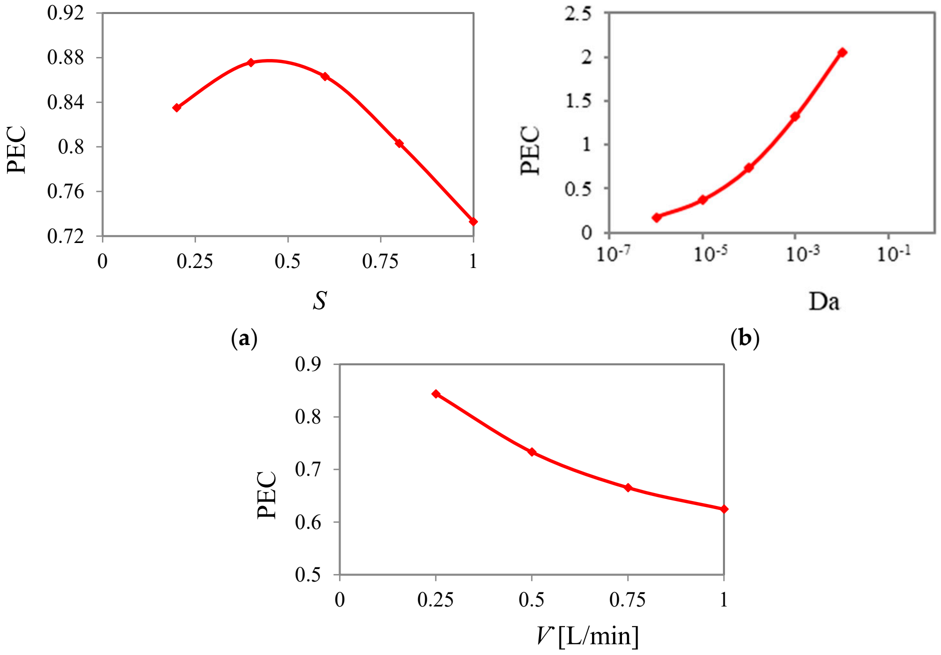

(**a**) (**b**)

(**c**)

Figure 9. Plot of performance evaluation criteria (PEC), as a function of (**a**) the channel fill ratio (S), (**b**) Darcy number (Da), and (**c**) volumetric flow rate ($\dot{V}$).

Next, the effect of volumetric flow rates ($\dot{V}$) on the values of the PEC was evaluated, and the results are shown in Figure 9c. This figure shows that the PEC follow the same trend as that of the friction factor. The value of the PEC is evaluated with respect to the empty channel case (i.e., $S = 0$) at the same value of $\dot{V}$. For example, the PEC are evaluated for a volumetric flow rate of 0.25 L/min in an empty channel. A decreasing trend is clearly observed in Figure 9c, which shows the highest value of the PEC at very low flow rates and low values of the PEC at higher flow rates. The figure shows that the value of the PEC is highest at a volumetric flow rate of 250 mL/min, and it decreases in a monotonous manner at higher flow rates. The value of the PEC is observed to be about 0.84, 0.73, 0.67, and 0.63, corresponding to value of flow rates of 250, 500, 750, and 1000 mL/min, respectively. This is due to the fact that at higher flow rates, the friction factor (f) for the empty channel decreases, while the value of the Nusselt number increases. This combination leads to an overall decrease in the value of the PEC at higher flow rates. It is also interesting to note that in Figure 9c, the value of the PEC is always observed to be lower than 1. This indicates that the increase in pressure drop penalty is greater than the augmentation in the Nusselt number. Hence, to attain a higher value of the PEC, a lower value of the volumetric flow rate is preferable.

4.4. Comparison Between LTE (Local Thermal Equilibrium) and LTNE (Local Thermal Non-Equilibrium)

In the numerical study conducted so far, the underlying assumption has been that the solid (porous metallic foam) and liquid (working fluid) are in local thermal equilibrium. In simpler words, it has been assumed that the working fluid and solid-phase temperature approach a local equilibrium temperature instantly. With this assumption, a mean temperature can be considered that accounts for both the solid and working fluid temperature field. This assumption has been used widely even after several decades of porous medium analysis, wherein a single energy equation serves for both the phases. However, in reality, the heat dissipation from the solid (porous foam) to the working fluid is unsteady in nature, which contradicts the mean temperature assumption made in LTE modelling. Hence, the present sub-section aims to quantify the deviation between the LTE and LTNE (local thermal non-equilibrium) modelling. The comparison is performed in terms of isotherm contours, the non-dimensional temperature profile at the outlet and the Nusselt number evaluation under similar operating conditions. The LTNE model is more realistic and considers the energy balance of both phases separately. Hence, here, a two-equation approach is employed to provide solutions for the temperature fields within the solid and liquid regions separately. One equation takes care of the energy balance in the clear fluid flow region, while another energy equation accounts for the porous medium. However, it should also be noted that the LTNE approach is more complex and computationally expensive than the LTE approach. The numerical solvers and tolerances remain the same as discussed earlier.

With LTNE conditions, the governing equations for continuity and momentum remain the same as before, as can be seen in the equations for continuity and momentum. Only the single energy equation considered earlier needs to be replaced by two energy equations, shown as Equations (25) and (26). These equations represent the temperature fields for the solid phase and the fluid phases in the absence of internal heat generation for an isotropic and homogenous porous medium. The term indicated by the subscript "*f*" represents the fluid region, while the term indicated by the subscript "*s*" represents the solid phase of the porous medium.

Energy equation(s):

$$\rho C_p\left(u\frac{\partial T_f}{\partial x}+v\frac{\partial T_f}{\partial y}\right)=k_f\varepsilon\left(\frac{\partial^2 T_f}{\partial x^2}+\frac{\partial^2 T_f}{\partial y^2}\right)+h_{fs}a_{fs}\left(T_s-T_f\right) \tag{25}$$

$$k_s(1-\varepsilon)\left(\frac{\partial^2 T_s}{\partial x^2}+\frac{\partial^2 T_s}{\partial y^2}\right)-h_{fs}a_{fs}\left(T_s-T_f\right)=0 \tag{26}$$

In these equations, h_{fs} and a_{fs} represent the interfacial heat transfer coefficient occurring between the fluid and solid phases and the specific surface area, respectively. These terms account for the convective mode of heat transfer occurring at the solid–fluid interface. The expressions for h_{fs} and a_{fs} are as follows [46,47].

$$h_{fs}=\frac{k_f}{d_p}\left(2+\mathrm{Pr}_f^{0.33}\left(\frac{u\mathrm{d}_p}{\nu}\right)^{0.6}\right) \tag{27}$$

$$a_{fs}=\frac{6(1-\varepsilon)}{d_p} \tag{28}$$

The numerical simulations are run with the LTNE approach for a completely filled channel corresponding to the S = 1 case, and the isotherm contours are compared with the LTE case. The Da considered in the numerical comparison was equal to 10^{-2}, corresponding to a particle diameter (d_p) of 0.55 mm. The values of h_{fs} and a_{fs} that were calculated were found to be equal to 7760.83 W/m^{2}K and 218.18 m^{-1}, with values of k_f = 0.6 W/mK, u = 0.009 m/s, and Pr = 6.13. The isotherms obtained in both dimensional and non-dimensional forms are shown in Figure 10 for the two cases (LTE and LTNE). The isotherms were non-dimensionalized by dividing the temperature by the difference in the absorber plate outlet temperature and the fluid inlet temperature. As seen in this figure, the isotherm contours for both LTE and LTNE show an almost similar trend. The isotherm contours drop in a monotonous manner from the top absorber plate to the bottom insulated surface in both cases. In LTNE, the isotherm contours extend backward in the flow direction, representing a somewhat parabolic profile. In contrast, in the case of LTE, the isotherm contours follow a kind of half parabola path. Hence, in the LTNE approach, a slightly higher temperature is obtained near the bottom insulated surface compared to the LTE case. However, the mean or bulk temperature at the outlet for both cases is in close agreement, with the value of 305.7 K for the LTNE case and 306.8 K for the LTE case. The deviation between the two approaches was found to be 0.35%.

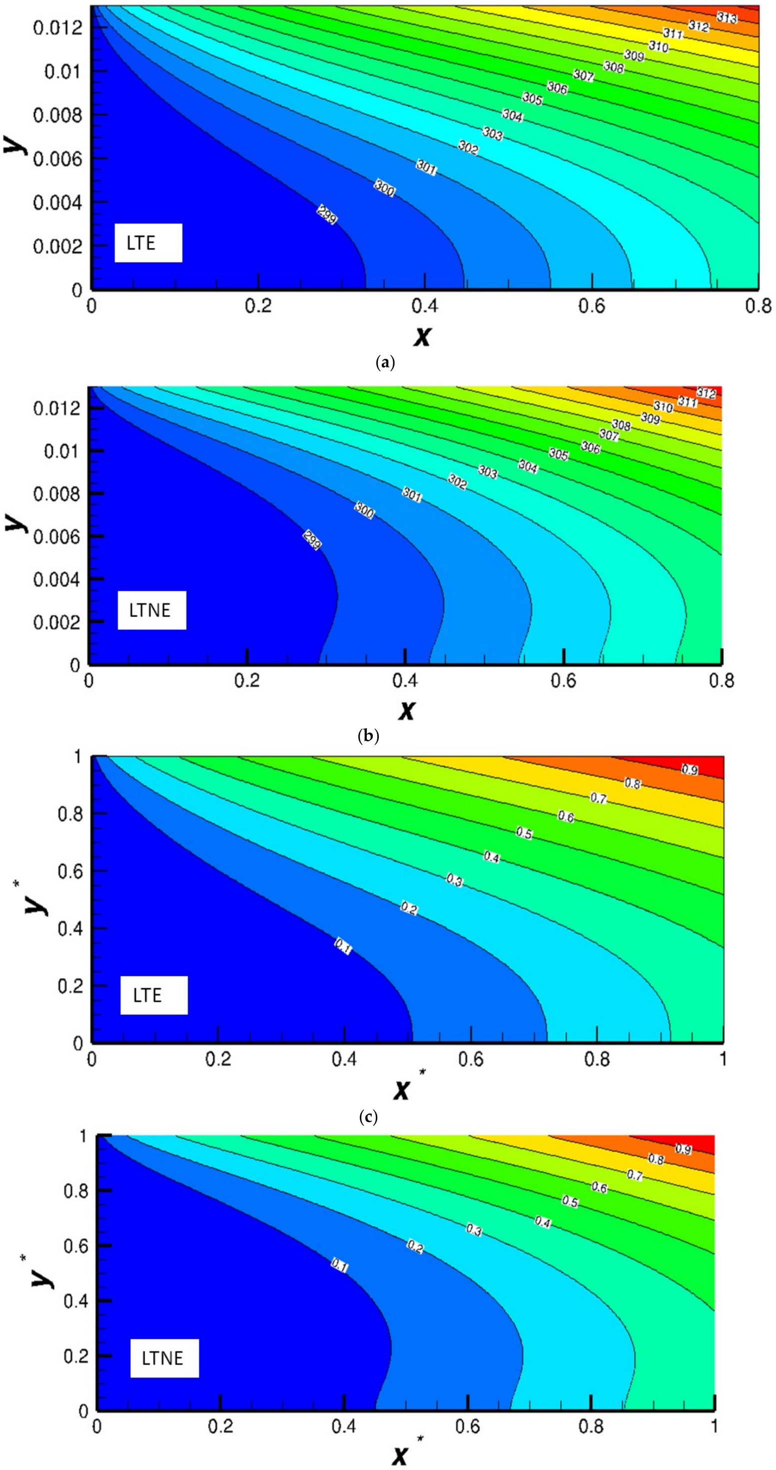

(a)

(b)

(c)

(d)

Figure 10. A comparison of isotherm contours between the LTE and LTNE results (at S = 1). The results are presented in both the dimensional form (**a**,**b**) and non-dimensional form (**c**,**d**).

Further ahead, the temperature profile in the non-dimensional form was plotted at the outlet for both LTNE and LTE cases under similar operating conditions. The graphical representation of the temperature profile is as shown in Figure 11. The non-dimensionalization is performed considering the fluid temperature at the inlet and the absorber plate temperature at the outlet. As shown in Figure 11, for both cases, the temperature profile follows a half parabola, with the value of around 0.38 and 0.28 at the bottom insulated surface for LTNE and LTE, respectively. In the case of LTE, a higher temperature than LTNE is obtained at the upper half of the channel, while a lower temperature than LTNE is obtained at the lower wall of the channel near the insulated surface, as seen earlier in the isotherm contours as well. However, the overall effect produces approximately the same averaged outlet temperature (with the deviation being around 0.35%). Similarly, the maximum deviation between the non-dimensional temperature profiles between LTE and LTNE was found to be less than 10%. Finally, the Nusselt number was evaluated for both LTE and LTNE approaches (at channel outlets), and these values were found to be equal to 27.63 and 29.87, respectively, with a deviation of about 8.1%.

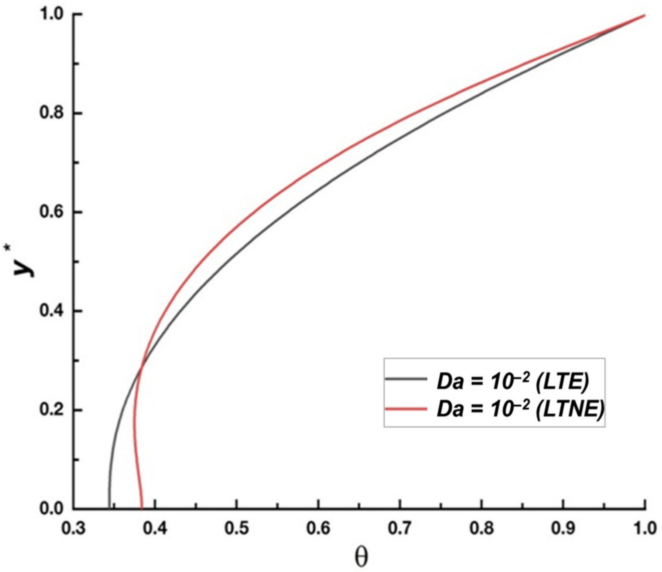

Figure 11. A comparison between the outlet temperature profiles of LTE and LTNE (corresponding to $S = 1$ and $\mathrm{Da} = 10^{-2}$).

5. Conclusions

In the present study, the influence of porous foam on the flow pattern and thermal performance of an FPC is presented. Numerical simulations based on the finite volume method are performed on the open-source tool OpenFOAM. The numerical arrangement considered consists of a rectangular cross-sectional channel with a length of 0.8 m and height of 0.013 m and porous copper foam integrated in the centre of the channel along the entire length. The numerical code is written by modifying the SIMPLE algorithm in the OpenFOAM repository to solve the pressure, velocity, and temperature terms in governing equations. The porous region is modelled using the Darcy–Brinkman–Forchheimer extended model. The porous foam is considered to be homogenous and isotropic, and therefore, uniform porosity is assumed. This study is conducted with the assumption of local thermal equilibrium (LTE) between the solid matrix and the working fluid. In addition, the superficial velocity is considered in the porous region in the numerical code. The validation of the written code is performed, and a satisfactory agreement with results from the existing research literature is presented. From the numerical simulations, the results are as follows:

- The influence of the height of the porous foam placed at the centre of the channel is studied. The local Nusselt number is investigated for six different cases corresponding to the values of S = 0, 0.2, 0.4, 0.6, 0.8, and 1 and a Da of 10^{-4}. The bulk or mean temperature at the outlet reaches a maximum value of 306.81 K at $S = 1$ and corresponds to the highest Nusselt number (Nu) value of 28.85.
- The effect of the permeability of the porous foam (with $S = 1$) is studied by varying Da in the range from 10^{-6} to 10^{-2}, while the volumetric flow rate ($\dot{V}$) varies from 0.25 L/min to 1 L/min. Maximum enhancement in the Nusselt number of 29.2 and 31.05 is obtained at Da equal to 10^{-6} and a volumetric flow rate ($\dot{V}$) of 1 L/min.
- It is found that the friction factor is highest when the channel is completely filled with porous foam ($S = 1$) equal to 1.61 compared to 0.004 for an empty channel case ($S = 0$). Hence, a rise in pressure drop is evident with the insertion of porous foam in the channel, causing an increase in pumping power.
- The performance evaluation criteria (PEC) are also calculated corresponding to different values of S and their variation with Da and $\dot{V}$ is quantified. It is observed that the PEC first increase with an increase in the height of porous foam up to S = 0.4, reach a maximum value of 0.875, and then decrease with a further increase in the height of porous foam up to S = 1. The PEC show an increasing trend with an increase in Da and reach a maximum value of 2.05, corresponding to Da = 10^{-2}.

Author Contributions: Conceptualization, V.K., M.P. and H.T.; Methodology, V.K., A.S.K., M.P. and H.T.; Software, H.T. and V.K.; Validation, V.K., A.S.K. and H.T.; Formal analysis, M.P. and H.T.; Investigation, V.K., A.S.K. and H.T.; Data curation, V.K., A.S.K.; Writing—original draft, V.K., A.S.K., M.P. and H.T.; Writing—review & editing, V.K., A.S.K., M.P. and H.T.; Supervision, H.T.; Project administration, H.T. All authors have read and agreed to the published version of the manuscript.

Funding: This research received no external funding.

Institutional Review Board Statement: Not applicable.

Informed Consent Statement: Not applicable.

Data Availability Statement: The raw data supporting the conclusions of this article will be made available by the authors on request.

Acknowledgments: The authors wish to acknowledge the support provided by the Department of Mechanical Engineering at the Indian Institute of Technology Ropar.

Conflicts of Interest: The authors declare no conflicts of interest.

Nomenclature

Symbols	
a	Specific surface area [m^{-1}]
A	Area [m^2]
C	Forchheimer coefficient [1/m]
D	Diameter [m]
Da	Darcy number [-]
f	Friction factor [-]
h	Heat transfer coefficient [W/m^{2}K]
H	Channel height [m]
J	Solar insolation [W/m^2]
k	Thermal conductivity of material [W/mK]
L	Channel length [m]
Nu	Nusselt number [-]
P	Pressure [kg/ms^2]

p	Perimeter [m]
Pr	Prandtl number [-]
q	Heat flux [W/m^2]
Re	Reynolds' number [-]
S	Channel fill ratio (=H_p/H)
$\bar{s}$	Velocity of fluid in porous region [m/s]
t	Time [s]
T	Temperature [K]
U	Fluid velocity [m/s]
u	x-component of velocity [m/s]
v	y-component of velocity [m/s]
$\dot{V}$	Volumetric flow rate [L/min]
Vol	Volume of the porous medium [m^3]
Greek symbols	
δ	Hydraulic conductivity of the porous medium [m/s]
ρ	Density [kg/m^3]
μ	Dynamic viscosity [kg/ms]
ν	Kinematic viscosity [m^2/s]
ε	Porosity
κ	Permeability of material [m^2]
σ	Stefan–Boltzmann constant
θ	Non-dimensional temperature
Subscripts	
eff	Effective
e	Empty channel case
f	Fluid property
fs	Fluid–solid interface
h	Hydraulic
in	Inlet value
m	Mean value
p	Pore region
r	Radiative
s	Solid matrix property
w	Wall
Abbreviations	
CFD	Computational fluid dynamics
HTF	Heat transfer fluid
FPC	Flat-plate collector
IR	Infrared
LTE	Local thermal equilibrium
LTNE	Local thermal non-equilibrium
PEC	Performance evaluation criteria
PPI	Pores per inch
RTE	Radiative transfer equation

References

1. Tian, Y.; Zhao, C.Y. A review of solar collectors and thermal energy storage in solar thermal applications. *Appl. Energy* **2013**, *104*, 538–553. [CrossRef]
2. Chen, M.; He, Y.; Zhu, J.; Kim, D.R. Enhancement of photo-thermal conversion using gold nanofluids with different particle sizes. *Energy Convers. Manag.* **2016**, *112*, 21–30. [CrossRef]
3. Taylor, R.; Coulombe, S.; Otanicar, T.; Phelan, P.; Gunawan, A.; Lv, W.; Rosengarten, G.; Prasher, R.; Tyagi, H. Small particles, big impacts: A review of the diverse applications of nanofluids. *J. Appl. Phys.* **2013**, *113*, 011301. [CrossRef]
4. Menbari, A.; Alemrajabi, A.A.; Rezaei, A. Heat transfer analysis and the effect of CuO/Water nanofluid on direct absorption concentrating solar collector. *Appl. Therm. Eng.* **2016**, *104*, 176–183. [CrossRef]

5. Tyagi, H.; Phelan, P.; Prasher, R. Predicted Efficiency of a Low-Temperature Nanofluid-Based Direct Absorption Solar Collector. *J. Sol. Energy Eng.* **2009**, *131*, 041004. [CrossRef]
6. Sharafeldin, M.A.; Gróf, G. Experimental investigation of flat plate solar collector using CeO_2-water nanofluid. *Energy Convers. Manag.* **2018**, *155*, 32–41. [CrossRef]
7. Michael, J.J.; Iniyan, S. Performance of copper oxide/water nanofluid in a flat plate solar water heater under natural and forced circulations. *Energy Convers. Manag.* **2015**, *95*, 160–169. [CrossRef]
8. Moghadam, A.J.; Farzane-Gord, M.; Sajadi, M.; Hoseyn-Zadeh, M. Effects of CuO/water nanofluid on the efficiency of a flat-plate solar collector. *Exp. Therm. Fluid Sci.* **2014**, *58*, 9–14. [CrossRef]
9. Verma, S.K.; Tiwari, A.K.; Chauhan, D.S. Experimental evaluation of flat plate solar collector using nanofluids. *Energy Convers. Manag.* **2017**, *134*, 103–115. [CrossRef]
10. Kulkarni, V.; Kashyap, A.S.; Pal, M.; Tyagi, H. Numerical Analysis of a Flat Plate Solar Collector Integrated with Porous Copper Foam. In Proceedings of the 26th National and 4th International ISHMT-ASTFE Heat and Mass Transfer Conference, IIT Madras, Chennai, India, 17–20 December 2021; Begellhouse: Danbury, CT, USA, 2022; pp. 645–651. [CrossRef]
11. Anirudh, K.; Dhinakaran, S. On the onset of vortex shedding past a two-dimensional porous square cylinder. *J. Wind Eng. Ind. Aerodyn.* **2018**, *179*, 200–214. [CrossRef]
12. Dhinakaran, S.; Ponmozhi, J. Heat transfer from a permeable square cylinder to a flowing fluid. *Energy Convers. Manag.* **2011**, *52*, 2170–2182. [CrossRef]
13. Srivastava, P.K.; Agrawal, S.K.; Pandey, M.K. Enhanced heat and mass transfer in a solar still with a porous-fin lattice Basin. *J. Enhanc. Heat Transf.* **2013**, *20*, 491–498. [CrossRef]
14. Wu, H.W.; Wang, R.H. Mixed convective heat transfer past a heated square porous cylinder in a horizontal channel with varying channel height. *J. Heat Transf.* **2011**, *133*, 022503. [CrossRef]
15. Vijaybabu, T.R.; Anirudh, K.; Dhinakaran, S. Mixed convective heat transfer from a permeable square cylinder: A lattice Boltzmann analysis. *Int. J. Heat Mass Transf.* **2017**, *115*, 854–870. [CrossRef]
16. Guerroudj, N.; Kahalerras, H. Mixed convection in a channel provided with heated porous blocks of various shapes. *Energy Convers. Manag.* **2010**, *51*, 505–517. [CrossRef]
17. Chen, C.C.; Huang, P.C.; Hwang, H.Y. Enhanced forced convective cooling of heat sources by metal-foam porous layers. *Int. J. Heat Mass Transf.* **2013**, *58*, 356–373. [CrossRef]
18. Chikh, S.; Boumedien, A.; Bouhadef, K.; Lauriat, G. Analysis of fluid flow and heat transfer in a channel with intermittent heated porous blocks. *Heat Mass Transf. Stoffuebertragung* **1998**, *33*, 405–413. [CrossRef]
19. Lansing, F.L.; Clarke, V.; Reynolds, R. A high performance porous flat-plate solar collector. *Energy* **1979**, *4*, 685–694. [CrossRef]
20. Chen, C.C.; Huang, P.C. Numerical study of heat transfer enhancement for a novel flat-plate solar water collector using metal-foam blocks. *Int. J. Heat Mass Transf.* **2012**, *55*, 6734–6756. [CrossRef]
21. Bovand, M.; Rashidi, S.; Esfahani, J.A. Heat transfer enhancement and pressure drop penalty in porous solar heaters: Numerical simulations. *Sol. Energy* **2016**, *123*, 145–159. [CrossRef]
22. Chen, Z.; Gu, M.; Peng, D. Heat transfer performance analysis of a solar flat-plate collector with an integrated metal foam porous structure filled with paraffin. *Appl. Therm. Eng.* **2010**, *30*, 1967–1973. [CrossRef]
23. Rashidi, S.; Bovand, M.; Esfahani, J.A. Heat transfer enhancement and pressure drop penalty in porous solar heat exchangers: A sensitivity analysis. *Energy Convers. Manag.* **2015**, *103*, 726–738. [CrossRef]
24. Kumar, A.; Saini, R.P.; Saini, J.S. Performance evaluation of discrete multi V-down pattern rib solar air channel. *J. Enhanc. Heat Transf.* **2016**, *23*, 393–411. [CrossRef]
25. Anirudh, K.; Dhinakaran, S. Numerical study on performance improvement of a flat-plate solar collector filled with porous foam. *Renew. Energy* **2020**, *147*, 1704–1717. [CrossRef]
26. Chaurasiya, S.K.; Singh, S. Thermohydraulic Performance Analysis of a Solar Air Heater Design Employing Wavy Corrugated Plates and Impinging Air Jet Array. *J. Enhanc. Heat Transf.* **2023**, *30*, 75–104. [CrossRef]
27. Xia, Y.; Lin, X.; Cheng, Z.; Xie, F.; Huang, J. Numerical Study on the Enhanced Thermal Performance of the Porous Media-Assisted Flat-Plate Solar Collector. *Int. J. Energy Res.* **2023**, *2023*, 2244771. [CrossRef]
28. Dhavale, A.A.; Lele, M.M. Numerical investigations on the impact of metallic foam configurations on heat transfer in double tube heat exchanger: A parametric approach. *Numer. Heat Transf. Part A Appl.* **2024**, 1–53. [CrossRef]
29. Al-Chlaihawi, K.; Hasan, M.; Ekaid, A. Optimizing heat transfer within a rectangular channel through intermittent metal foam block configurations: A numerical study. *Heat Transf.* **2025**, *54*, 716–748. [CrossRef]
30. Variji, N.; Hosseini Imeni, S.Z.; Siavashi, M. Multi-objective optimization of porous foam structure to enhance energy performance of flat plate solar collectors. *J. Therm. Anal. Calorim.* **2024**, *149*, 3543–3559. [CrossRef]
31. Lin, X.; Xia, Y.; Cheng, Z.; Liu, X.; Fu, Y.; Li, L.; Zhou, W. Thermal Performance Analysis of Porous Foam-Assisted Flat-Plate Solar Collectors with Nanofluids. *Sustainability* **2024**, *16*, 693. [CrossRef]

32. Raccurt, O.; Disdier, A.; Bourdon, D.; Donnola, S.; Stollo, A.; Gioconia, A. Study of the Stability of a Selective Solar Absorber Coating under Air and High Temperature Conditions. *Energy Procedia* **2015**, *69*, 1551–1557. [CrossRef]
33. Narasimhan, A. *Essentials of Heat and Fluid Flow in Porous Media*; CRC: Boca Raton, CA, USA, 2013.
34. Khullar, V.; Bhalla, V.; Tyagi, H. Potential Heat Transfer Fluids (Nanofluids) for Direct Volumetric Absorption-Based Solar Thermal Systems. *J. Therm. Sci. Eng. Appl.* **2018**, *10*, 011009. [CrossRef]
35. Ritchie, I.T.; Window, B. Applications of thin graded-index films to solar absorbers. *Appl. Opt.* **1977**, *16*, 1438. [CrossRef] [PubMed]
36. Bear, J.; Bachmat, Y. *Introduction to Modeling of Transport Phenomena in Porous Media*; Springer: Dordrecht, The Netherlands, 1990. [CrossRef]
37. Anirudh, K.; Dhinakaran, S. Performance improvement of a flat-plate solar collector by inserting intermittent porous blocks. *Renew. Energy* **2020**, *145*, 428–441. [CrossRef]
38. Modest, M.F. *Radiative Heat Transfer*; Academic Press: Cambridge, MA, USA, 2013. [CrossRef]
39. Cintolesi, C.; Nilsson, H.; Petronio, A.; Armenio, V. Numerical simulation of conjugate heat transfer and surface radiative heat transfer using the P1thermal radiation model: Parametric study in benchmark cases. *Int. J. Heat Mass Transf.* **2017**, *107*, 956–971. [CrossRef]
40. Derby, J.J.; Brandon, S.; Salinger, A.G. The diffusion and P1 approximations for modeling buoyant flow of an optically thick fluid. *Int. J. Heat Mass Transf.* **1998**, *41*, 1405–1415. [CrossRef]
41. Xiong, Q.; Baychev, T.G.; Jivkov, A.P. Review of pore network modelling of porous media: Experimental characterisations, network constructions and applications to reactive transport. *J. Contam. Hydrol.* **2016**, *192*, 101–117. [CrossRef]
42. Saedodin, S.; Zamzamian, S.A.H.; Nimvari, M.E.; Wongwises, S.; Jouybari, H.J. Performance evaluation of a flat-plate solar collector filled with porous metal foam: Experimental and numerical analysis. *Energy Convers. Manag.* **2017**, *153*, 278–287. [CrossRef]
43. Bhattacharya, A.; Calmidi, V.V.; Mahajan, R.L. Thermophysical properties of high porosity metal foams. *Int. J. Heat Mass Transf.* **2002**, *45*, 1017–1031. [CrossRef]
44. Morosuk, T.V. Entropy generation in conduits filled with porous medium totally and partially. *Int. J. Heat Mass Transf.* **2005**, *48*, 2548–2560. [CrossRef]
45. Mohamad, A.A. Heat transfer enhancements in heat exchangers fitted with porous media Part I: Constant wall temperature. *Int. J. Therm. Sci.* **2003**, *42*, 385–395. [CrossRef]
46. Foudhil, W.; Dhifaoui, B.; Ben Jabrallah, S.; Belghith, A.; Corriou, J.P. Numerical and experimental study of convective heat transfer in a vertical porous channel using a non-equilibrium model. *J. Porous Media* **2012**, *15*, 531–547. [CrossRef]
47. Al-Sumaily, G.F.; Nakayama, A.; Sheridan, J.; Thompson, M.C. The effect of porous media particle size on forced convection from a circular cylinder without assuming local thermal equilibrium between phases. *Int. J. Heat Mass Transf.* **2012**, *55*, 3366–3378. [CrossRef]